Available online at www.sciencedirect.com
SCIENCE DIRECT®
Journal of Sound and Vibration 269 (2004) 913–931
JOURNAL OF SOUND AND VIBRATION
www.elsevier.com/locate/jsvi

Sensors and control of a space-based six-axis vibration isolation system

G.S. Hauge[a,*], M.E. Campbell[b]

[a] Department of Mechanical Engineering, University of Washington, Box 352400, Seattle, WA 98195-2400, USA
[b] Department of Aeronautics and Astronautics, University of Washington, Box 352400, Seattle WA 98195-2400, USA

Received 20 December 2001; accepted 14 January 2003

Abstract

A study of several critical aspects of six-axis hexapods used for space-based vibration isolation is conducted. These issues include the choice of sensor and subsequent control architecture, the predictability and limitations of the experimental system dynamics and therefore the ultimate robustness of the design, and the achievement of performance and robustness requirements for future space-based interferometers. The cross-axis dynamics, which is a limiting factor in achievable performance, is shown to be dependent on the internal wiring of the struts. A two-sensor control architecture is shown to be the only sensor suite to meet the performance and robustness requirements of future interferometers. Many of the insights in this paper are derived from experimental evidence of a full, six-axis hexapod system.

1. Introduction

Many future space systems will require very quiet environments for precision pointing. Space interferometry [1,2], spacecraft laser communications [3], and other precision spacecraft are examples of applications where nanometer level of motion stability is required. To achieve these stringent requirements, a variety of spacecraft designs and control architectures will be used. One of the most important technologies is vibration isolation between the precision instrument and disturbance sources, such as reaction wheels, solar array drives, cryocoolers, and other noisy machinery. This work addresses the stringent requirements of future space-based interferometers,

*Corresponding author. Sibley School of Mechanical and Aerospace Engineering, Cornell University, 208 Upson Hall, Ithaca, NY 14853-7501, USA. Tel.: +1-607-255-4268; fax: +1607-255-1222.
E-mail address: mc288@cornell.edu (G.S. Hauge).

0022-460X/03/$ - see front matter
doi:10.1016/S0022-460X(03)00206-2

as described in Ref. [16]. Here, the primary motion requirement is a −20 dB reduction on all six axes of vibration (three translation and three rotation) between 5 and 20 Hz.

To achieve the extremely high optical stability levels in six degrees of freedom of a spacecraft, a cubic hexapod, or Stewart platform [3–5] is envisioned for a six-axis active vibration isolation. The cubic hexapod is a logical approach because it decouples into six axes of vibration, which eases both the analysis of vibration as well as control design. A number of Stewart platforms have been implemented by different research groups around the country to investigate the problems involved in a six-axis vibration isolation. Each system is designed to a somewhat different mission. For a summary of these hexapods, the reader should refer to Ref. [6].

Using lessons learned from past approaches, Hood Technology Corporation (HT) and the University of Washington (UW) have designed, built, and tested a unique hexapod design for spaceborne interferometry missions [6]. The HT/UW system (Fig. 1) is unique in its low corner frequency (which can be changed with a variety of flexures), large actuator stroke (±5 mm for precision pointing), and number of sensors (each of the six struts has a three-axis load cell, a base and a payload geophone and a LVDT). Elastomer flexures, rather than steel, reduce lateral stiffness and improve passive performance at payload resonance (damping) and at frequencies greater than 100 Hz. But they also require that the 15.5 kg payload is offset in 1 g using long, soft linear springs. With this great flexibility in hardware options, a variety of sensor architectures and hardware studies can easily be implemented and compared. Ref. [6] provides a hardware summary of the HT/UW hexapod, as well as the initial control results and integrated isolation/pointing experiments.

As a background to six-axis vibration isolation using six-axis hexapods, there are several past and on-going studies. A general trade study of vibration isolation sensors, actuators and configurations was conducted by Blackwood and von Flotow [7]. A theoretical hexapod sensor study was conducted by Spanos and Rahman [8]. In general, force sensors such as load cells, work well to measure vibration, but have difficulty with cross-axis dynamics. Inertial sensors, on the other hand, do not have this cross-axis limitation, but are usually more sensitive to payload and

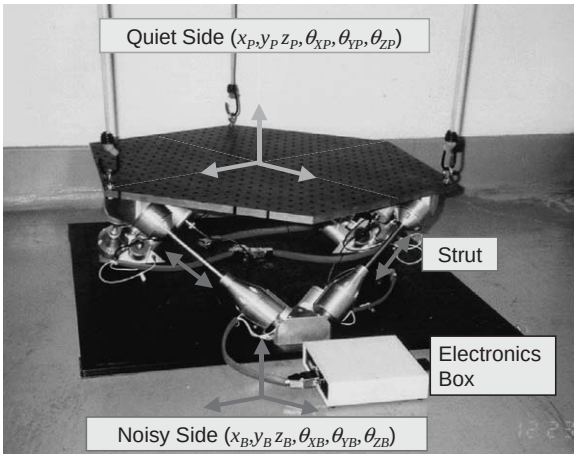

Fig. 1. The HT/UW hexapod for six-axes active vibration isolation. Base and payload geophones are mounted separately in parallel with the strut.

base dynamics and are more difficult to control due to the non-collocated nature of the sensor and actuator. Although previous experimental research in hexapod vibration isolation has utilized both force [9–12] and inertial sensor feedback [13,14] individually, no experimental comparison of these sensors or associated architectures has been reported. The HT/UW hexapod allows this type of comparison.

Force sensors typically work well because they are not as sensitive to payload and base dynamics [15], but are limited in performance by a low-frequency zero pair resulting from the cross-axial stiffness. This zero pair has confused many researchers because it is very sensitive, occasionally becoming non-minimum phase [6,8]. The zero pair is the current limitation in performance using load cell sensors, as opposed to the theoretical rigor of the algorithms [8]. The work presented here studies this zero pair experimentally and makes several conclusions that are important to future hexapod designs.

The objectives of this paper are to: (1) develop insight into the performance limiting zero pair in the load cell transfer function, (2) compare load cell, inertial, and combinations of sensors for six-axis isolation, and (3) achieve the strict performance objectives of future spaceborne interferometry missions. As will be shown, the first objective is a direct result of understanding physically, through experimental evidence, why the performance limiting, low-frequency zero pair is not predictable. The second objective attempts to compare, in an unbiased manner using the same HT/UW hexapod, different sensors and architectures for six-axis isolation. The third objective is met by using the insight from the first two objectives in the control design, which yields a two sensor per strut control architecture.

This paper begins with a discussion of the performance objectives of isolation in spaceborne interferometry, and a summary of the models and control approaches used. Next, the cross-axis dynamics are studied, specifically focusing on understanding the low-frequency zero pair in the load cell transfer function. The variations are shown to be a direct result of a non-linearity from the strut internal wiring. Lastly, a set of control results are shown, including force (load cell), inertial (geophone), and a combination of the two. The two-sensor control architecture is shown to be the only sensor suite to meet the performance and robustness requirements of future interferometers.

2. Modelling approach

2.1. Performance objective

The performance objective of this work is based on the stringent requirements of future space-based interferometers [16], and is shown to be modelled as a frequency domain metric. The two most important factors that lead to these requirements are the pointing and vibration limit of the science instrument and the command and disturbance created by a set of reaction wheels. These wheels are used to point the spacecraft at low frequency; therefore, the (low-frequency) reaction wheel torque must fully transfer through the hexapod. At higher frequencies, the reaction wheels cause noises (both harmonic and broadband) that disturb the sensitive telescope; therefore, the torques at higher frequencies must be isolated from the instrument. These two requirements are the focus of much of the isolation work for spaceborne interferometers.

The general concept of transmissibility, or unitless vibration from a noisy side to a quiet side, has been used for many years as a measure of scalar performance for isolation designs. Attempting to develop a scalar performance for six-axis designs, such as in the general hexapod, is a good approach because of its simplicity, ease in understanding, and ease in working with control approaches. For hexapod systems, a 6×6 transfer function matrix, $G_{6\times6}(s)$, can be defined from the six base velocity (or acceleration) inputs to six payload velocity (or acceleration) outputs

$$\begin{bmatrix} \dot{X}_P \\ \dot{\Theta}_P \end{bmatrix} = [G_{6x6}(s)] \begin{bmatrix} \dot{X}_B \\ \dot{\Theta}_P \end{bmatrix}, \tag{1}$$

where $X_P = \begin{bmatrix} x_P & y_P & z_P \end{bmatrix}^{\mathrm{T}}$ is the three-axis inertial position of the center of the payload side, and $\Theta_P = \begin{bmatrix} \theta_{XP} & \theta_{YP} & \theta_{ZP} \end{bmatrix}^{\mathrm{T}}$ is the three-axis rotation of the center of the payload side, with similar definitions for the base positions X_B and rotations Θ_B. The co-ordinate systems are defined in Fig. 1.

The scalar six-axis transmissibility as a function of frequency is then defined as

$$T(\omega) = \sqrt{\mathrm{trace}(G(\mathrm{j}\omega)G^*(\mathrm{j}\omega))}. \tag{2}$$

This metric can be plotted and interpreted just as traditional transmissibility functions are, but with the added understanding of its underlying six-axis definition. The stringent motion requirements for space-based interferometers can now be written more formally as two requirements:

*REQ*1: Low-frequency (pointing)—keep $T(\omega)$ within ± 3 dB in the 0–1.5 Hz range, or

$$-3\,\mathrm{dB} < |T(\omega)| < 3\,\mathrm{dB}, \quad \omega = (0 - 1.5\,\mathrm{Hz})\,2\pi.$$

*REQ*2: High-frequency (disturbance rejection)—keep $T(\omega)$ below –20 dB in the 5–20 Hz range

$$|T(\omega)| < -20\,\mathrm{dB}, \quad \omega = (5 - 20\,\mathrm{Hz})\,2\pi.$$

Maintaining the –20 dB reduction above 20 Hz, while not a specific requirement, is also a consideration in the design. Both of these requirements are common in isolation design; the challenge here lies in the small frequency separation between the two, the low isolation requirement (5 Hz), and the six-axis design.

The transmissibility can then be used to define a scalar performance metric J to be used in common control design approaches. The two-norm of both the transmissibility and the 6×6 transfer function matrix, $G_{6\times6}(s)$, is written as

$$J = \|G_{6x6}\|_2^2 = \frac{1}{2\pi}\int_{-\infty}^{\infty} (T(\omega))2\,\mathrm{d}\omega = \frac{1}{2\pi}\int_{-\infty}^{\infty} \mathrm{trace}(G(\mathrm{j}\omega)G^*(\mathrm{j}\omega))\,\mathrm{d}\omega. \tag{3}$$

A final, but equally important performance consideration is robustness in the control design. Robustness can be measured in many ways, such as with additive or multiplicative errors, parametric (such as internal model parameter) or non-parametric (such as high-frequency payload dynamics) uncertainty, and repeatability. In this work, given the experimental focus, robustness is measured as the ability of a design to perform repeatably in experiment, and the minimization of transmissibility amplification (Bode's "pop") outside the performance region.

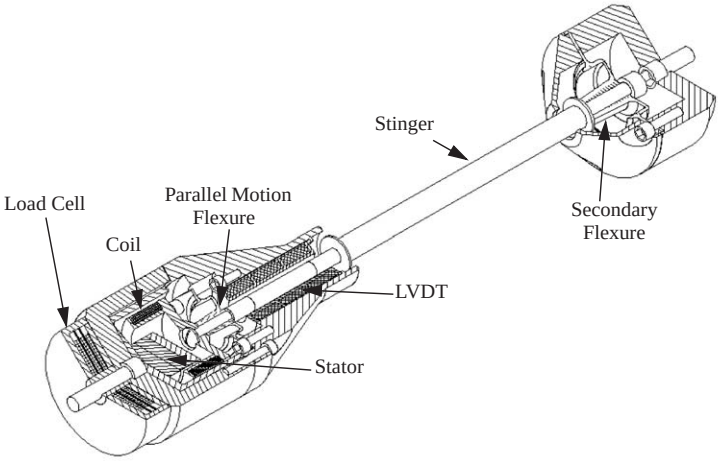

Fig. 2. Cutaway view of a single HT/UW strut.

2.2. Modelling of the six-axis hexapod

Fig. 2 shows a cut-away view of one of the six identical struts. Both elastomer flexures are shown, along with the placement of the sensors and actuators. The parallel motion flexure is attached near the center of percussion of the strut, i.e., near the attachment of the voice coil. The secondary flexure is attached at the bottom of the strut. More details on this unique design for interferometers can be found in Ref. [6].

This work utilizes two models. First, a full six-axis model, including all cross-axial stiffness and damping, strut finite elements, and sensors and actuators is available. This model, which contains 70–100 states depending on the level of desired accuracy, was used only in the final controller analysis. Two typical transfer functions for this model are shown in Figs. 8 and 10, where the model is overlaid with experimental data for the voice coil to load cell and geophone sensors, each showing excellent correlation.

The primary model used in this work is that of a single strut axis. This is common for cubic hexapods because of their decoupling into six single-axis systems. Fig. 3 shows a simple, but accurate model of a single strut, which can be written as follows:

$$\begin{bmatrix} m_B & & \\ & m_S & \\ & & m_P \end{bmatrix} \begin{bmatrix} \ddot{x}_B \\ \ddot{x}_S \\ \ddot{x}_P \end{bmatrix} + \begin{bmatrix} c_1 + c_c & -c_1 & -c_c \\ -c_1 & c_1 + c_2 & -c_2 \\ -c_c & -c_2 & c_2 + c_c \end{bmatrix} \begin{bmatrix} \dot{x}_B \\ \dot{x}_S \\ \dot{x}_P \end{bmatrix}$$
$$+ \begin{bmatrix} k_1 + k_c & -k_1 & -k_c \\ -k_1 & k_1 + k_2 & -k_2 \\ -k_c & -k_2 & k_2 + k_c \end{bmatrix} \begin{bmatrix} x_B \\ x_S \\ x_P \end{bmatrix} = \begin{bmatrix} 1 \\ -1 \\ 0 \end{bmatrix} f_{VC}$$
$$\begin{bmatrix} v_B \\ v_P \\ y_{LC} \end{bmatrix} = \begin{bmatrix} 0 & 1 & 0 \\ 0 & 0 & 1 \\ 0 & -c_2 & c_2 \end{bmatrix} \begin{bmatrix} \dot{x}_B \\ \dot{x}_S \\ \dot{x}_P \end{bmatrix} + \begin{bmatrix} 0 & 0 & 0 \\ 0 & 0 & 0 \\ 0 & -k_2 & k_2 \end{bmatrix} \begin{bmatrix} x_B \\ x_S \\ x_P \end{bmatrix}, \tag{4}$$

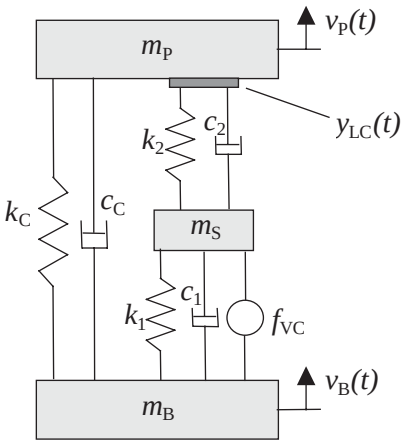

Fig. 3. Single strut model with sensor locations. The model parameters are given as: $k_C = 760\,\mathrm{N/m}$—cross-axial stiffness in the hexapod; $c_C = 12.1\,\mathrm{N\,s/m}$—cross-axial damping; $k_1 = 3,900\,\mathrm{N/m}$—stiffness of primary flexure; $c_1 = 22.3\,\mathrm{N\,s/m}$—damping of primary flexure; $k_2 = 52{,}000\,\mathrm{N/m}$—stiffness of secondary flexure; $c_2 = 5.20\,\mathrm{N\,s/m}$—damping of secondary flexure; $m_b = 75.0\,\mathrm{kg}$—mass base; $m_s = 0.254\,\mathrm{kg}$—mass of strut stinger; $m_p = 15.5\,\mathrm{kg}$—mass of payload; $y_{LC}(t)$—force measurement (load cell); $v_p(t)$—payload velocity measurement (geophone); $v_B(t)$—base velocity measurement (geophone); f_{VC}—force actuator input.

where B, S, and P refer to the base, stinger, and payload, respectively. In this model, k_1 and c_1 refer to the primary (parallel motion) flexure, k_2 and c_2 as the secondary flexure, and k_C, c_C, as the cross-axial stiffness and damping in the hexapod. The cross-axial stiffness is a result of the rotational, bending and sheer stiffness of the secondary flexures of the other five axes, along with wiring and payload suspension (in 1 g). These connections create an additional vibration path from the payload to the base that cannot be measured within the voice coil to load cell transfer function. Also included in the model are sensor dynamics for the geophone sensors, which can be written as a second order high pass filter with an 11 Hz corner frequency, or

$$\begin{aligned}
&\ddot{x}_{VB} + [2 \cdot 0.5(11 \cdot 2\pi)]\dot{x}_{VB} + [11 \cdot 2\pi]^2 \dot{x}_{VB} = [11 \cdot 2\pi]^2 v_B,\\
&y_{VB} = v_B - x_{VB} - [2 \cdot 0.5/(11 \cdot 2\pi)]\dot{x}_{VB},\\
&\ddot{x}_{VP} + [2 \cdot 0.5(11 \cdot 2\pi)]\dot{x}_{VP} + [11 \cdot 2\pi]^2 \dot{x}_{VP} = [11 \cdot 2\pi]^2 v_P,\\
&y_{VP} = v_P - x_{VP} - [2 \cdot 0.5/(11 \cdot 2\pi)]\dot{x}_{VP},
\end{aligned} \tag{5}$$

where $v_{(\cdot)}$ refers to the ideal inertial velocity, $x_{(\cdot)}$ to the geophone internal state, and $y_{(\cdot)}$ to the actual geophone measurement.

The single-axis model has 10 states including sensor dynamics of the geophone. The transfer functions for this model are nearly identical to those shown for the full six-axis model in Figs. 8 and 10, except there is only one payload frequency at 2.9 Hz. In fact, when the full six-axis model is reduced to a single axis, 10 state model using standard techniques [17], it is identical to that presented in Eqs. (4) and (5). The payload and base dynamics are not modelled here because they are greater than 110 Hz, and the focus of this work is on understanding the basic isolator system and the cross-axis dynamics, as well as the required sensor topology. An obvious next step in this research would be to integrate and model realistic base and payload dynamics. Watters [15] and Blackwood [7] provide in depth descriptions of how to approach this important phase.

3. Predictability of the dynamics: internal wiring effects

One of the most important issues in control design using a force sensor (load cell) is the appearance of a low frequency, lightly damped zero pair in the voice coil to load cell transfer function. The zero pair occurs at the resonant frequency of the payload mass and the feed through stiffness (sum of the cross-axial, umbilical wiring, suspension) and is usually control limiting [6,8,12]. The zero pair occasionally produces a puzzling effect, not previously explained. In experiments, both the UW and JPL [9] unexpectedly found this low-frequency zero pair to be non-minimum phase. In addition, the location and damping of the zero pair were not repeatable in day-to-day experiments. Not being able to predict or understand why this zero pair is non-minimum phase has caused concern over its use as a sensor for control design.

After extensive study of the zero phenomenon, the authors have concluded that the non-minimum phase behavior is due to a non-linearity imposed on the system by the wiring of the voice coil. The wires, especially those powering the voice coils, make the voice coil to load cell transfer functions very sensitive at low frequencies. This is best shown in a series of single strut experiments, summarized in Figs. 4–6. Fig. 4 shows several wire arrangements, while Fig. 5 shows the voice coil to load cell transfer functions for each case. Different wire arrangements result in very different phase behavior near the zero frequency. Not only does the phase behavior change, but large frequency and damping changes can be seen as well. This is a result of several influences, such as the wire rubbing or pushing against the inside of the strut can. The most important influence, however, appears to be internal tension in the wire. Case A1, where the tension is quite high, causes the zero to move to a very low frequency, strongly increases damping, and produces the non-minimum phase behavior.

Case B is a special case. The wire is resting against the rubber flexure inside the can. This drastically increases the umbilical stiffness, thus increasing the zero frequency. Case C is an attempt to obtain an ideal wire arrangement. The wire is in a position where it undergoes minimum bending as the voice coil moves. This creates a case where the zero pair frequency is minimum phase, and at a very low frequency, which is a result the remaining suspension system and cross-axial stiffness.

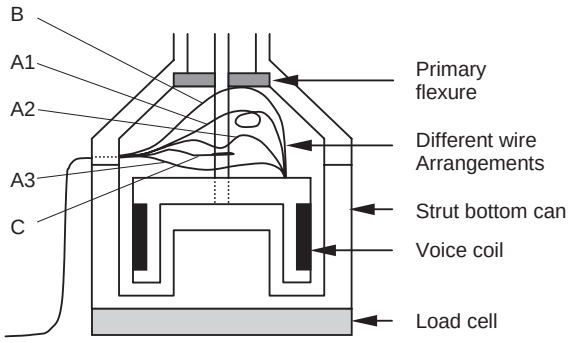

Fig. 4. Different wire arrangements for the wires powering voice coil: (A1) large bending in umbilical, looped arrangement, low tension in umbilical; (A2) medium bending in umbilical, medium tension in umbilical; (A3) medium bending in umbilical, high tension in umbilical; (B) large bending in umbilical, wire is resting against the rubber flexure inside can; (C) low bending in umbilical, low tension in umbilical.

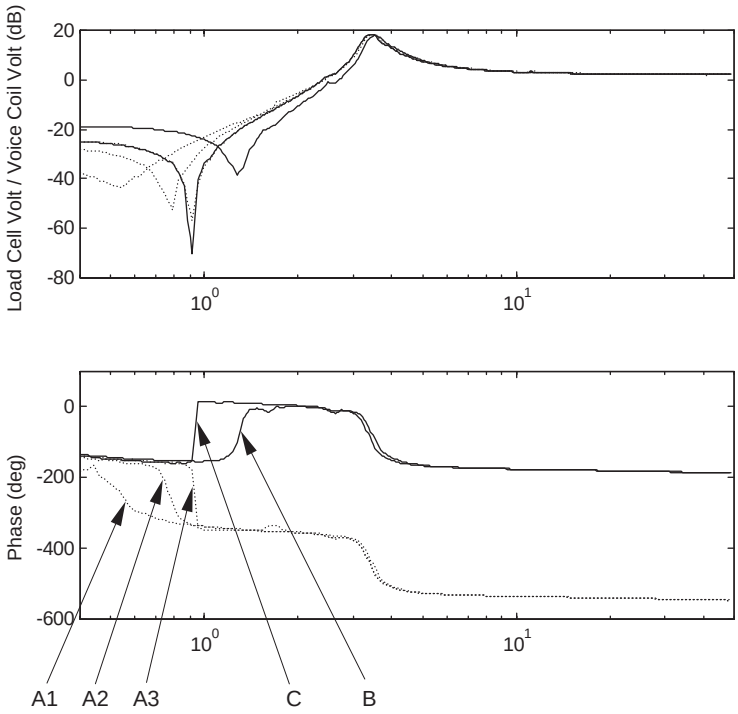

Fig. 5. Voice coil to load cell transfer functions for five different wire arrangements: (A1) zero pair at very low-frequency and non-minimum phase, highly damped; (A2) zero pair at low-frequency and non-minimum phase, medium damped; (A3) zero pair at medium frequency and non-minimum phase, lightly damped; (B) zero pair at high-frequency and minimum phase, medium damped; (C) zero pair at medium frequency and minimum phase, lightly damped.

Because the source of the non-minimum phase behavior is a non-linearity within the system from the voice coil wire arrangements, sine sweep time responses of the system allow insight into the relationship between the non-linearity and the phase behavior. Fig. 6 shows the time response of the load cell output for a 1 Hz voice coil input (left), and the magnitude and phase for the full sine sweep from 0.4 to 1 Hz (right). As the wiring tension increases, the load cell output signal becomes distorted, and the phase of the zero pair becomes non-minimum phase.

The lightly damped, non-minimum phase behavior is similar to that of the tilt gravity zero, where gravity influences the sensor more so than the passive dynamics, thereby creating a minimum or non-minimum phase low-frequency zero pair. The cable routing affect is, in fact, modelled in a very similar manner. The differences in the cable routing case are (1) the zero pair is sensitive to the changing wiring configurations, and (2) the sensitivity can be seen in many different configurations, not just the horizontal configuration usually seen in the case of a tilt gravity zero.

There are many benefits of a cubic hexapod, but the predictability of the cross-axis dynamics and this zero pair ultimately limit the load cell-based controllers. Because the internal wiring runs from the voice coil to the strut can (Fig. 4), its ideal configuration is parallel with the primary elastomer flexure, such that it only affects the passive corner frequency. Yet, as Fig. 5 shows, the wiring also affects the zero pair (i.e., cross-axial stiffness). The ideal strut, with the conductor

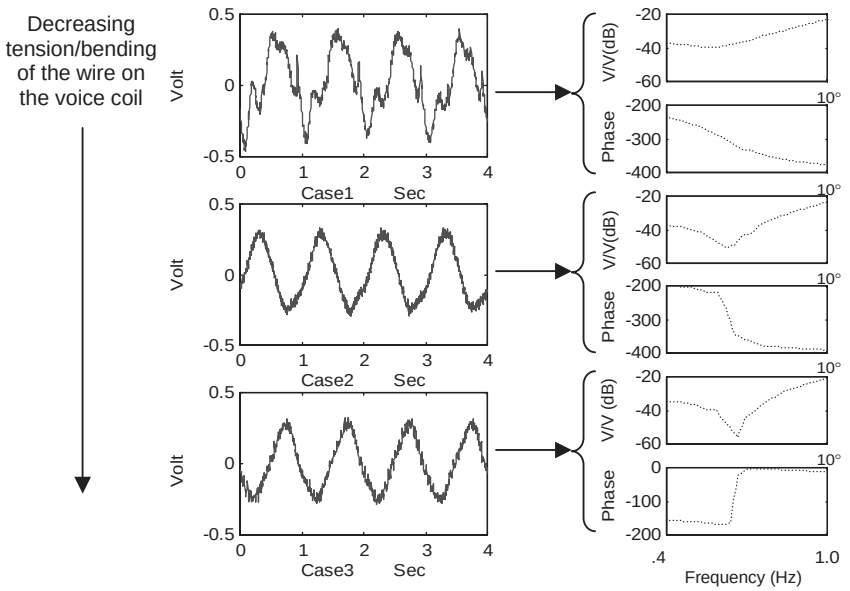

Fig. 6. Load cell output at 1 Hz for a sinusoidal voice coil input and corresponding magnitude and phase from 0.4 to 1 Hz.

powering the voice coil integrated as a part of, or truly in parallel with, the main flexure, can be achieved in several ways. First, if metal flexures are used, the supply current to the voice coil could simply be led through the flexures themselves or the wire could be made as an integrated part of the flexure (using a flexible conducting material which does not undergo permanent deformation during operation). Second, a conducting soft spring material could be used for wiring, which is then run symmetrically out from the voice coil.

4. Control approach

Control design for this system can be simple or complex because of the many choices such as the model type (full or single-axis), sensor suite (load cell or geophone or a combination), and control algorithm (classical, multivariable, robust, or adaptive). As shown in Ref. [6], the use of multivariable and robust control on the full 6×6 hexapod does not improve performance over single-axis designs. This is because (1) the full model does not capture the cross-axis dynamics well enough for these techniques, and (2) the location of the low-frequency zero pair in the load cell transfer functions is not repeatable. In fact, when robust control approaches are applied and uncertainty in the cross-axis dynamics and low-frequency zero pair is added into the problem, the controller tends toward a decoupled design (i.e., six single-axis controllers). Thus, it makes sense to develop single-axis controllers, combine them into a full six-axis controller, and evaluate the full controller in terms of stability and robustness. This is the approach taken here because it allows this work to focus on the sensor selection and topology.

The control approaches used here include two linear quadratic techniques, one of which is a design method that is robust to dynamic uncertainties. While there are certainly other robust

techniques, most appear to give similar solutions because of the simplicity of the system (10 states). Also because of the single-axis simplicity, the controller structure can easily be interpreted in a classical manner.

The first technique is the stochastic linear quadratic Gaussian (LQG) controller [18]. The original model in Eqs. (4)–(5) can be integrated into a single-axis, state space model of the form

$$\dot{x} = Ax + B_u u + B_w w, \quad y = C_y x + D_u u + v, \quad z = C_z x, \tag{6}$$

where the state x, sensor y, input u, performance z, and disturbance w are defined as

$$x = [x_B \;\; x_S \;\; x_P \;\; \dot{x}_B \;\; \dot{x}_S \;\; \dot{x}_P \;\; x_{VB} \;\; \dot{x}_{VB} \;\; x_{VP} \;\; \dot{x}_{VP}]^{\mathrm{T}},$$
$$y = [y_{LC} \;\; y_{VP}]^{\mathrm{T}}, \quad u = [f_{LC}], \quad z = [v_P], \quad w = [V_B],$$

and where v is the sensor noise. Given a white noise disturbance and sensor noise with intensity Σ_{ww} and Σ_{vv}, the LQG controller minimizes the two norm of the performance and input, or

$$J = E\left[z^2 + \rho_1 u^2\right], \tag{7}$$

where $E[\ ]$ denotes expectation, and ρ_1 is a scalar that allows the designer to trade between minimizing the performance versus minimizing the input. The single-axis controller, $K_{SA}(s)$, is then defined as

$$K_{SA}(s) = F[sI - A + B_u F + HC_y]^{-1} H, \tag{8}$$

where F and H are found from the solutions to two algebraic Ricatti equations

$$A^{\mathrm{T}} S + SA + I - \frac{1}{\rho_1} S B_u B_u^{\mathrm{T}} S = 0, \quad F = \frac{1}{\rho_1} B_u^{\mathrm{T}} S,$$
$$AQ + QA^{\mathrm{T}} + B_w \Sigma_{ww} B_w^{\mathrm{T}} - QC_y^{\mathrm{T}} \Sigma_{vv}^{-1} C_y Q = 0, \quad H = QC_y^{\mathrm{T}} \Sigma_{vv}^{-1}. \tag{9}$$

Once the single-axis controller is developed, the controller for the full six-axis hexapod can be integrated as

$$\begin{bmatrix} u_1 \\ u_2 \\ u_3 \\ u_4 \\ u_5 \\ u_6 \end{bmatrix} = \begin{bmatrix} K_{SA}(s) & & & & & \\ & K_{SA}(s) & & & & \\ & & K_{SA}(s) & & & \\ & & & K_{SA}(s) & & \\ & & & & K_{SA}(s) & \\ & & & & & K_{SA}(s) \end{bmatrix} \begin{bmatrix} y_1 \\ y_2 \\ y_3 \\ y_4 \\ y_5 \\ y_6 \end{bmatrix}. \tag{10}$$

A robust controller can easily be developed in this framework by adding sensitivity parameters to the cost function, or

$$J = E\left[z^2 + \rho_{si}\left(\frac{dz}{d\eta_i}\right)^2 + \rho_1 u^2\right], \tag{11}$$

where ρ_{si} refers to the weighting on the parameter η_i. These additions then create minor modifications to the Riccati equation in Eq. (9). This controller is called the sensitivity weighted LQG controller (SWLQG), and has been show to adequately address robustness in flexible dynamic systems. For more information on the solution to this controller, please see Ref. [19].

The control approach used here was to first use LQG to achieve the best z versus u tradeoff (i.e., finding ρ_1). Then, SWLQG was used to robustify the controller to uncertainties in the dynamics, such as the low-frequency zero pair and the high-frequency unmodelled dynamics. All control designs were then evaluated (stability and performance) on the full six-axis model. This was done using a variety of methods, but the best approach was to close the loop using open loop data, and evaluate the closed loop performance and Nyquist diagrams [20]. This technique has worked well in the past as a less conservative, albeit non-guaranteed approach to analysis. In general, because of the decoupling, the stability robustness of all controllers was quite good.

4.1. Sensor suite

An important contribution of this work is the experimental comparison of different sensor suite results on hexapod systems, specifically focusing on isolation for space-based interferometry. As such, it is important to understand the typical characteristics of these sensors (primarily based on a priori results). This is shown in Table 1.

The load cell sensor is collocated and dual (i.e., both relative) with respect to the voice coil actuator, as defined in Ref. [21]. This implies an alternating pole-zero plant, as shown in Fig. 8. The geophone sensor is non-collocated and non-dual (inertial as compared to the relative voice coil), which implies a transfer function that rolls off more quickly. This is shown by the phase drop-off in Fig. 10. The load cell sensor is limited at low frequency due to the very sensitive, lightly damped zero pair resulting from the cross-axial stiffness (Fig. 8). The geophone sensor is more sensitive to payload and base dynamics as compared to the load cell sensor, as shown by the 110 Hz payload mode in Fig. 10.

When considering the ability of a sensor–actuator pair to improve performance, Campbell and Crawley developed a test to understand how well a sensor–actuator pair can minimize a given performance metric [21]. This test is summarized as follows: for a general system with a single disturbance w, performance z, input u, and output y, the open loop single-input–single-output (SISO) transfer functions can be written as

$$\begin{bmatrix} z \\ y \end{bmatrix} = \begin{bmatrix} G(s)_{zw} & G(s)_{zu} \\ G(s)_{yw} & G(s)_{yu} \end{bmatrix} \begin{bmatrix} w \\ u \end{bmatrix}. \tag{12}$$

Table 1
Typical characteristics of sensors used for isolation in hexapod systems

	Load cell	Geophone
Type	Relative	Inertial
Relationship with voice coil	Collocated and dual	Non-collocated and non-dual
Open loop transfer function	Alternating poles/zeros (+)	Large phase drops (−)
Limitation from low-frequency zero pair	Yes (−)	No (+)
Sensitive to payload/base dynamics	No (+)	Yes (−)
Good pairing from S–A test	No (−)	Yes (+)
Best frequency range	High (low-freq. zero limitations)	Low (high-freq. roll-off limitations)

Given a SISO controller $u = -K(s)y$, the closed loop disturbance to performance transfer function (w to z) can be written as

$$\left[\frac{z}{w}\right]_{CL} = \frac{G(s)_{zw} + K(G(s)_{zw}G(s)_{yu} - G(s)_{zu}G(s)_{yw})}{1 + KG(s)_{yu}}. \tag{13}$$

In the case presented here, Eq. (13) defines the closed loop transmissibility. The test states that in order to significantly reduce the closed loop transfer function (w to z) such that the backbone of the transfer function is reduced, a high gain controller must be used. The justification of this test, shown in more detail in Ref. [21], is that if the term $[G(s)_{zw}G(s)_{yu} - G(s)_{zu}G(s)_{yw}]$ in the numerator of Eq. (13) is large, there is no "robust" approach for the controller to reduce the closed loop transfer function. For instance, in examining Eq. (13), the most obvious approach is to invert and cancel the $[G(s)_{zw}G(s)_{yu} - G(s)_{zu}G(s)_{yw}]$ term. But, this breaks down in a realistic setting (i.e., with noise, uncertainty, etc.). This was shown in both analysis and test [21]. As shown in Ref. [21], the only control approach that can reduce the backbone of Eq. (13) and achieve significant performance improvement is to use a high gain controller, *provided* the term $[G(s)_{zw}G(s)_{yu} - G(s)_{zu}G(s)_{yw}]$ is small.

This test can be developed in the frequency domain by comparing the w to z transfer function with and without a high gain controller Eq. (13) with $K(s)$ large, $K(s) = 0$ which is open loop). The following must be true for y, u to be an acceptable pair for high gain control (i.e., pass the test):

$$\left|\frac{G_{zw}(j\omega)G_{yu}(j\omega) - G_{zu}(j\omega)G_{yw}(j\omega)}{G_{yu}(j\omega)}\right| \ll |G_{zw}(j\omega)|. \tag{14}$$

For this work, w and z are the base and payload geophone sensors, u is the voice coil actuator, and y is the sensor (load cell or payload geophone). Therefore, the left side of Eq. (14) is the closed loop single-axis transmissibility with a high gain controller, and the right side is the open loop single-axis transmissibility. Fig. 7 shows the results of this test using experimental data for the load cell sensor placed at both the quiet (payload) and noisy (base) ends. The implications are: (1) placing the load cell on the payload side is a much better option for active isolation, and (2) the load cell sensor can achieve little performance improvement below 2 Hz, only modest results in the 2–5 Hz range, and good results above 5 Hz.

For the geophone sensor, the performance is measured directly (z and y are identical except for sensor noise). This implies that the left side of Eq. (14) is zero and the actuator–sensor test is satisfied at all frequencies. For this case, the closed loop performance in Eq. (13) simplifies to

$$\left[\frac{z}{w}\right]_{CL} = \frac{G(s)_{zw}}{1 + KG(s)_{yu}}. \tag{15}$$

In summary from Table 1, both sensors have their advantages and disadvantages. The observation that the load cell sensor works well at higher frequencies (limited by the low-frequency zero pair), while the geophone sensor works well at lower frequencies (limited by the roll-off of the open loop dynamics), has led to the sensor *combination* being an important design solution.

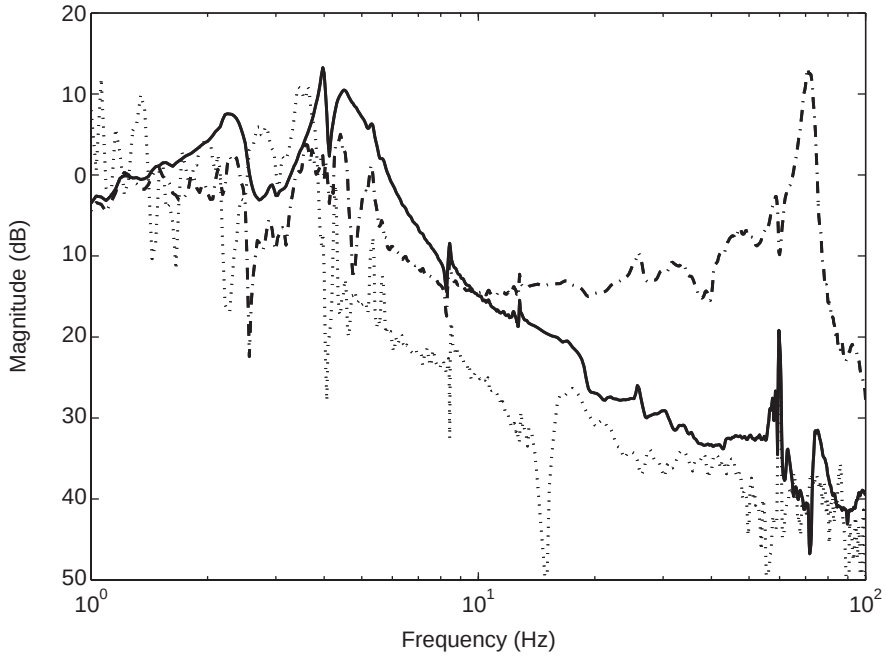

Fig. 7. Open loop transmissibility (solid) and the sensor–actuator test with the load cell on the noisy, base side (dash–dot) as compared to the quiet, payload side (dotted).

5. Experimental closed loop results

In this section, three sets of full six axis, experimental closed loop results are presented, each for a different sensor suite. First, load cell-based controllers and geophone-based controllers are presented. These single sensor designs are shown in order to (1) compare to other cases, and (2) show the evolution of the multi-sensor design. The final section discusses the combined load cell/geophone sensor, which is shown to be the only case capable of achieving the given performance and robustness requirements for future space-based interferometers. Results are presented in terms of the six-axis transmissibility; actual displacements were up to 3 mm in each axis.

5.1. Force feedback (load cell)

The difficulties in achieving closed loop performance (reduction of the transmissibility) using a load cell sensor are discussed previously, primarily focusing on the sensitive low-frequency zero pair. Achieving closed loop control using this sensor, even if this zero pair is minimum phase, is difficult. Consider the open loop, single-axis plant shown in Fig. 8. Because the low-frequency zero pair (0.8 Hz) is so close in frequency to the passive flexible modes (2.9 Hz), it is difficult to design a high loop gain and reduce the transmissibility to −20 dB by the 5 Hz requirement. Closed loop control using the load cell sensor is much easier if the zero pair/passive mode are separated by at least a decade in frequency. This can be achieved by reducing the cross-axis stiffness as much as possible, which has the effect of reducing the low-frequency gain, ΔG (Fig. 8). Note that in 0 g,

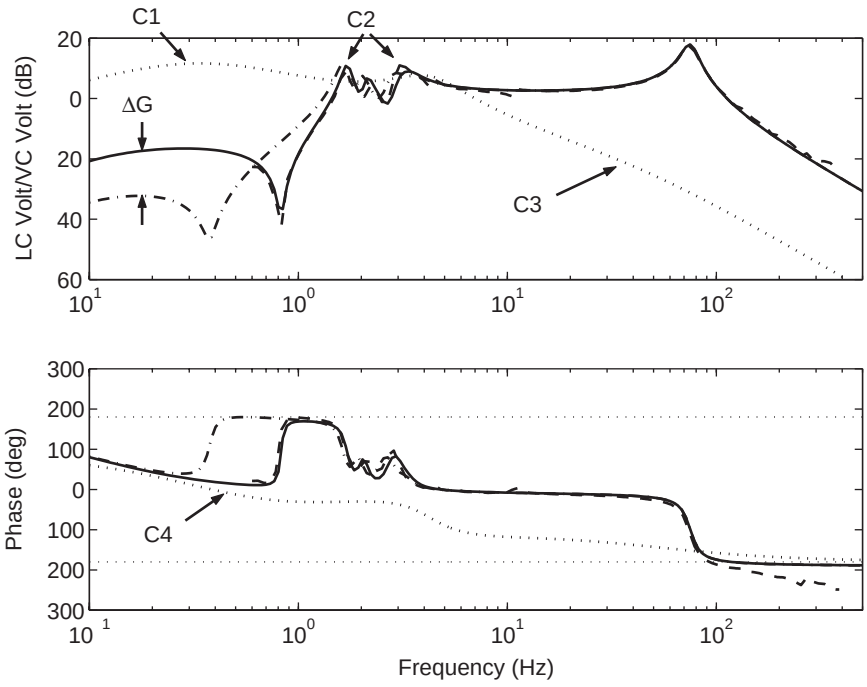

Fig. 8. Model (solid), model with a smaller cross-axial stiffness (dash–dot), experimental (dashed) voice coil to load cell plant transfer functions, and the high gain controller (dotted). The open loop dynamics include the low-frequency zero pair (at 0.38 and 0.81 Hz for two models), primary flexure modes (2–5 Hz), and the secondary flexure mode (70 Hz). The compensation includes: (C1) high pass filter to keep this excess gain below unity; (C2) inverted notch filter to boost gain within the control bandwidth; (C3) low pass filter to roll off the loop transfer function before secondary flexure resonance; (C4) lag filter to achieve good phase margin at lower cross over (1.2 Hz)

this zero pair would be at a lower frequency because a portion of the cross-axial stiffness due to the suspension system in 1 g would not be present.

Past control approaches for load cell sensors have attempted to increase the closed loop performance by inverting the low-frequency zero pair with a pair of compensator poles. In fact, the use of an LQG controller, which tends to invert dynamics [21], also uses this approach. But, when robustness is added to the controller, such as using the SWLQG approach, this controller inverted notch disappears and much of the performance is lost. Experimental evidence on the HT/UW hexapod has also shown the inverted notch solution to have repeatability problems (and thus not be robust) due to the sensitivity and low damping of the zero pair. It follows that the best load cell controller in terms of combined performance and robustness is designed to focus at frequencies at least a decade above the zero pair.

Fig. 8 shows the model and experimental voice coil to load cell transfer functions, and the compensation steps used in an attempt to meet the performance objectives. The controller uses a high pass filter to reduce the gain below the 0.8 Hz zero pair, a low-frequency lag filter to achieve good phase margin, an inverted notch in the 4 Hz region to reduce the transmissibility, and a low pass filter to roll the controller off before the 70 Hz corner of the secondary flexure. Fig. 9 shows the corresponding six-axis transmissibility. At frequencies below 2 Hz, the load cell controller does

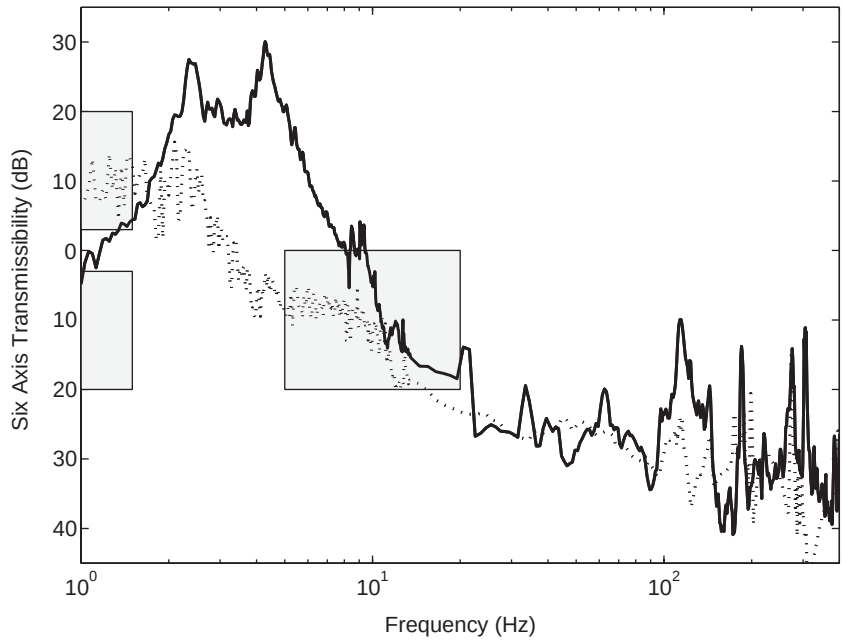

Fig. 9. Experimental open loop (solid) and closed loop (dotted) six-axis transmissibility using the load cell controller. The gray boxes indicate the performance requirements for space-based interferometry. The large amplification of the transmissibility at lower frequencies is due to phase limitations related to the low-frequency zero pair.

not meet the pointing performance requirement. This is a direct result of the small phase margin near the low-frequency zero pair. The controller also does not meet the 5–20 Hz requirement, although the transmissibility is less than −20 dB for most frequencies above 15 Hz.

5.2. *Inertial feedback (geophone)*

The inertial sensor is expected to perform better than the load cell sensor because it passes the actuator–sensor test at all frequencies. But, as will be shown, the non-collocated nature of the sensor–actuator pair provides a different set of limitations. Consider the voice coil to geophone transfer function shown in Fig. 10. This transfer function is dominated by three primary modes: the primary passive flexure in the 2–4 Hz region, the corner frequency of the geophone at 11 Hz, and the secondary strut flexure at 70 Hz. While the performance limiting low-frequency zero pair is not present, three 180° phase drops limit the ultimate bandwidth of the controller. The phase drops are a direct result of the voice coil actuator and geophone sensor being non-collocated [21]. In addition, payload plate modes at 110 and 120 Hz have coupled more easily into this transfer function.

Fig. 10 shows the model and experimental voice coil to geophone transfer functions, and the compensation steps used in an attempt to meet the performance objectives. The challenge for this sensor was achieving good phase margin at the higher frequency cross-over due to the phase roll-off of the three passive modes. The controller uses lag compensation at low frequency to achieve

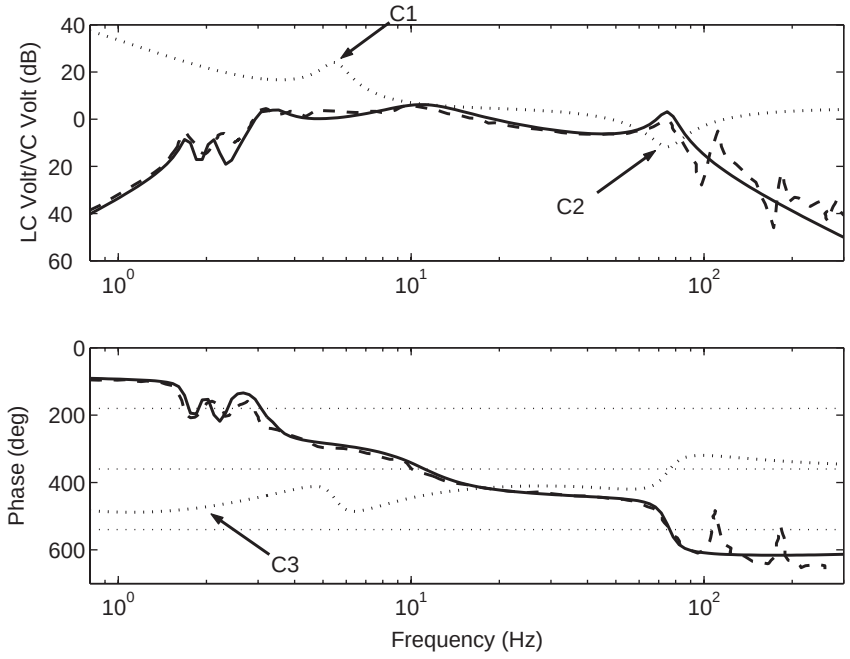

Fig. 10. Model (solid) and experimental (dashed) voice coil to geophone plant transfer functions, and the closed loop geophone-based controller (dotted). The open loop dynamics include the primary flexure modes (2–5 Hz), internal geophone corner (11 Hz), secondary flexure mode (70 Hz), and payload plate modes above 100 Hz. The compensation includes: (C1) an inverted notch filter to boost the gain within the control bandwidth; (C2) low pass filter to roll of the loop transfer function before the secondary flexure's resonance. Alternatively, a notch filter can be used to gain stabilize the resonance gain; (C3) extensive lag compensation to phase stabilize the loop near the lower cross over (1 Hz).

good phase margin, an inverted notch in the 5 Hz region to reduce the transmissibility, and a low pass filter/notch filter to roll off before the 70 Hz (secondary flexure) and 110 Hz (payload) dynamics. The experimental closed loop six-axis transmissibility is shown in Fig. 11, where it is compared to the combined load cell/geophone design (discussed in the next section). At low frequency, the transmissibility "pops" due to a low phase margin, thereby preventing the controller from meeting the performance requirement. The transmissibility is reduced to approximately –25 dB after 5 Hz, with the exception of the 20–70 Hz region where it is again amplified due to a low phase margin ($\sim 30^\circ$). While this controller appears to nearly achieve the performance objectives, the low phase margins and pop in the 1.5 Hz and 20–70 Hz regions indicate areas of robustness concern that should be addressed.

5.3. Combined force/velocity feedback (load cell/geophone)

The concept of a combined force/inertial feedback architecture is a natural extension of the previous two designs. The best controller uses the low-frequency performance advantages of the geophone sensor with the high-frequency robustness advantages of the load cell sensor. Using the robust SWLQG technique, a controller is designed for a single strut with two sensors (load cell

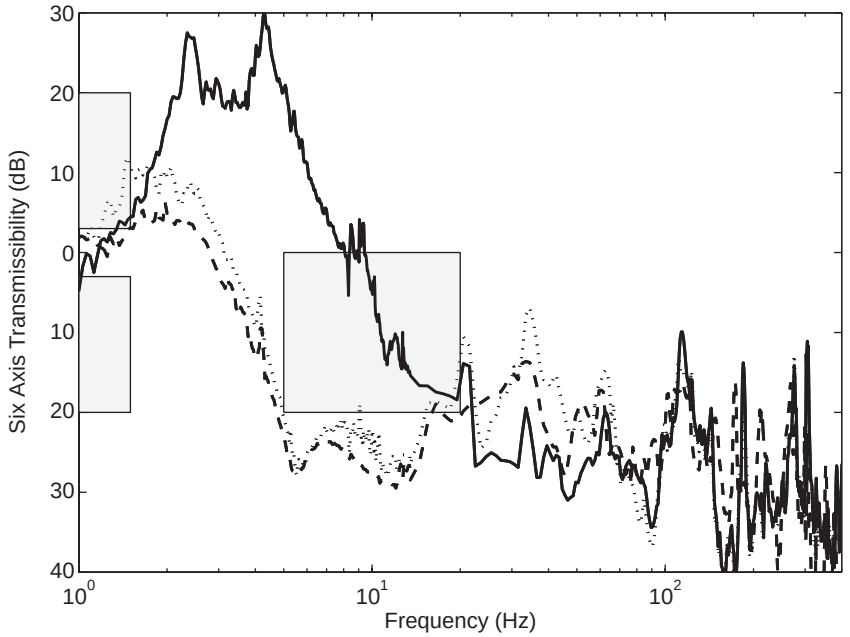

Fig. 11. Experimental open loop (solid) and closed loop six-axis transmissibility using the geophone only controller (dotted), and combined geophone/load cell controller (dashed). The gray boxes indicate the performance requirements for space-based interferometry. An inverted notch filter was used as a shaping filter to steeply drop the closed loop transmissibility in the 5 Hz range.

and geophone) and one actuator (voice coil). In this case, the mixture of the two sensors can be evaluated by defining the sensor noise intensity to be

$$\Sigma_{vv} = \begin{bmatrix} 1 & \\ & \rho_2 \end{bmatrix}, \tag{16}$$

where ρ_2 is a scalar parameter. As ρ_2 increases, the physical effect is that the payload geophone sensor appears noisier, and it is used less at higher frequencies. By iterating on the mixture of the two sensors using ρ_2, an integrated single-input–multiple-output (SIMO) controller is found. The controller is essentially decoupled into two SISO controllers because of their separate frequency ranges of interest. The interpretation of these two SISO controllers are as follows: (1) a geophone controller maintains the low-frequency transmissibility requirement (± 3 dB up to 1.5 Hz), and reduces the transmissibility in the 5–20 Hz region to –20 dB; (2) a load cell controller reduces the transmissibility and adds robustness/damping to the 1–90 Hz region. A single SIMO controller designed for each strut is then combined into a full MIMO (6 block SIMO) controller, as shown in Eq. (10). Fig. 11 shows closed loop performance for this controller. The benefits of this controller are apparent: (1) both the low and high-frequency performance objectives are met, (2) there is good robustness by not relying on the load cell sensor at low frequency, and (3) there is little pop at low or high frequency which indicate good gain margin and robustness.

6. Conclusions

Several important issues for achieving the strict performance and robustness requirements of future spaceborne interferometers were studied in this paper. Wire harnessing is a very important design issue, and must be carefully placed in order to increase plant predictability and reduce performance limiting, low-frequency zero effects. An inertial measurement is appropriate for controller designs when the cross-axial stiffness in the hexapod is relatively large. Force feedback is appropriate for flexible payloads, and if the cross-axial stiffness is very low such that the zero pair is at least a decade below the passive flexible modes of the hexapod. For the stringent performance and robustness requirements of future interferometry missions, multi-sensor (load cell and geophone) single-axis based controllers work well compared to other designs (such as the single sensor designs shown in this work and the multivariable robust designs shown in the references). The combined load cell/geophone controllers (1) achieve the low frequency (± 3 dB up to 1.5 Hz) and high frequency (–20 dB in 5–20 Hz region) performance requirements, (2) do not rely on the load cell sensor at low frequency where there are performance/robustness limiting zeros, and (3) minimize the pop or low phase margin/robustness issues at low or high frequency.

Acknowledgements

This work was funded from NASA Jet Propulsion Laboratory, Contract #1220951 with Mr. Ben Parvin as contract monitor.

References

[1] R. Danner, S. Unwin, Space Interferometry Mission, Taking the Measure of the Universe, Jet Propulsion Laboratory Publishing, Pasadena, CA, 1999.
[2] M. Shao, M. Colavita, Long-baseline optical and infrared stellar interferometry, Annual Review of Astronomy and Astrophysics 30 (1992) 457–498.
[3] R. Cobb, J. Sullivan, A. Das, L. Davis, T. Hyde, T. Davis, Z. Rahman, J. Spanos, Vibration isolation and suppression system for precision payloads in space, Smart Materials and Structures 8 (6) (1999) 798–812.
[4] D. Stewart, A Platform with six degrees of freedom, Proceedings of the Institution of Mechanical Engineers 180 (1965) 371–386.
[5] J. Geng, H. Leonard, Six degree-of-freedom active vibration control using the stewart platforms, IEEE Transactions on Control Systems Technology 2 (1) (1994) 45–53.
[6] D. Thayer, M. Campbell, J. Vagners, A. von Flotow, A unique six-axis active isolation system for spacecraft, American Institute of Aeronautics and Astronautics, Journal of Spacecraft and Rockets 39 (2) (2002) 206–212.
[7] G. Blackwood, A. von Flotow, Active control for vibration isolation despite resonant structural dynamics: a trade study of sensors, actuators and configurations, Proceedings of the Second Conference on Recent Advances in Active Control of Sound and Vibration, Blacksburg, VA, 1993.
[8] J. Spanos, Z. Rahman, Control concepts for active multi-axis vibration isolation, International Conference on Adaptive Structures, A96-25001 06-39, 1996, pp. 348–352.
[9] J. Spanos, Z. Rahman, G. Blackwood, A soft 6-axis active vibration isolator, Proceedings of the American Control Conference, 1995, pp. 412–416.
[10] Z. Rahman, J. Spanos, R. Laskin, A six axis vibration, suppression and steering system for space applications, Proceedings of the 35th AIAA Aerospace Sciences Meeting and Exhibit AIAA Paper 97-0245, 1997.

[11] Z. Rahman, J. Spanos, R. Laskin, Multi-axis Isolation, suppression and steering system for space observational applications, Society of Photo-Optical Instrumentation Engineers 3351 (1998) 73–81.
[12] T.T. Hyde, An experimental study of active isolation, Proceedings of the 38th AIAA/ASME/ASCE/AHS/ASC, Structures, Structural Dynamics and Materials Conference, Orlando, FL, 1997, pp. 1763–1773.
[13] E. Anderson, D.J. Leo, M.D. Holcomb, UltraQuiet platform for active vibration isolation, Proceedings Smart Structures and Integrated Systems 2717, San Diego, CA, 1996, pp. 436–451.
[14] J. Sullivan, Z. Rahman, R. Cobb, J. Spanos, Closed-loop performance of a vibration isolation and suppression system, Proceedings of the American Control Conference, Vol. 6, Albuquerque, NM, 1997, pp. 3974–3978.
[15] B.G. Watters, R.B. Coleman, G.L. Duckworth, E.F. Berkman, A perspective on active machinery isolation, Proceedings of the 27th Conference on Design and Control, Vol. 3, Austin, TX, 1988, pp. 2033–2038.
[16] J. Jandura, Analysis of hexapod isolator requirements necessary to meet sim opd requirements for astrometry and nulling, JPL Interoffice Memorandum (LJAN9705151), 1997.
[17] B.C. Moore, Principal component analysis of linear systems: controllability, observability, and model reduction, IEEE Transactions on Automatic Control AC-26 (1981) 17–32.
[18] H. Kwakernaak, R. Sivan, Linear Optimal Control Systems, Wiley-Interscience, New York, 1972.
[19] S. Grocott, J. How, D. Miller, Comparison of control techniques for robust performance on uncertain structural systems, Proceedings of the 1994 AIAA Conference of Guidance, Navigation, and Control, Scottsdale, AZ 1994, pp. 261–271.
[20] M. Campbell, S. Grocott, Parametric uncertainty model for control design and analysis, IEEE Transactions on Control Systems Technology 7 (1) (1999) 85–96.
[21] M.E. Campbell, E.F. Crawley, Classically rationalized low-order robust structural controllers, Journal of Guidance, Control, and Dynamics 21 (2) (1998) 296–306.